A Sampled-Grating Model of Moire Patterns from Digital Imaging

John Krumm and Steven A. Shafer

CMU-RI-TR-89-19

The Robotics Institute
Carnegie Mellon University
Pittsburgh, Pennsylvania 15213

July 1989

This research was supported by the Defense Advanced Research Projects Agency, DoD, through ARPA Order Number 4976, monitored by the Air Force Avionics Laboratory under Contract F33615-87-C-1499 and by the Jet Propulsion Laboratory, California Institute of Technology, sponsored by the National Aeronautics and Space Administration under Contract 957989. Any opinions, findings, conclusions or recommendations expressed in this publication are those of the authors and do not necessarily reflect the views of the United States Government or the Jet Propulsion Laboratory.

Contents

List of Figures

Abstract

Traditional "crossed-grating" moire, as well as newer "sampled-grating" (scanning) moire, have proven to be effective methods of shape measurement. There is speculation that the moire patterns of a sampled grating, which are due to aliasing, can be modeled with crossed gratings. We compare the two and show that while crossed gratings can correctly predict the frequencies of a sampled grating, they cannot correctly predict the amplitudes. We go on to formulate a new model which accounts for multiple stages of sampling and transmission, and show how neglecting multiple stages can lead to mistakes in moire analysis. We demonstrate our model with an experiment using a digital imaging system.

1 Introduction

Moire patterns can be caused by crossed gratings or by the discrete sampling of a single grating. The crossed-gratings case can be seen in everyday surroundings in layers of fences or screens. Figure 1 shows a contrived superposition of two crossed gratings that give rise to a moire pattern. If one of the crossed gratings is distorted, the moire pattern will be distorted, too. This phenomenon has been extensively exploited in metrology applications. One of the constituent gratings is projected onto a distorted object and observed through a second, flat grating. Since the resulting moire pattern is sensitive to small distortions in the object grating, accurate measurements of the object's shape can be derived. The object's shape is a function of the geometric layout of the original, undistorted gratings and the resulting moire pattern. Post [Pos67] has shown that an analysis of the profiles of the crossed gratings can be used to sharpen the moire fringe patterns, making it easier to track the fringes and thus easier to determine the shape of the object. Therefore, both the geometry and brightness profiles of the moire method are important to consider.

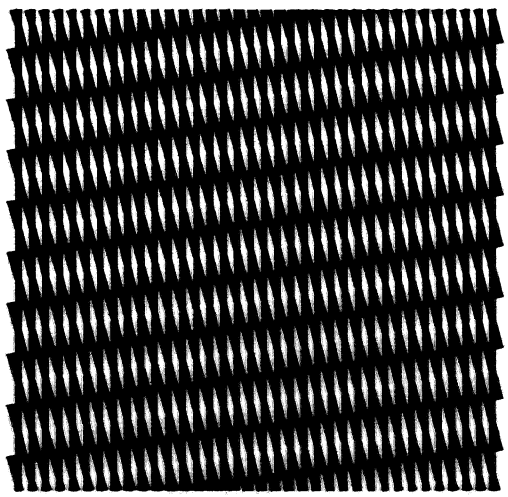

Figure 1: Crossed gratings making a moire pattern

Moire patterns can also be caused by aliasing in the discrete sampling of a single grating. The sampled-grating case can often be seen on television when a relatively high-spatial-frequency grating, say a striped shirt, is shown. Idesawa *et al.* [IYS77] have shown that the flat grating in traditional, crossed-grating, moire metrology can be replaced by a digital camera, still maintaining observable moire patterns using only a single, object grating. We will distinguish these two methods by calling the former "crossed-grating" moire and the later "sampled-grating" moire. The moire patterns from both methods appear similar, and it has been shown that sampled-grating moire can automate many time-consuming, subjective procedures of the traditional, crossed-grating paradigm [MSH88]. Idesawa *et al.* assert that the camera can be modeled by a second grating, thus allowing the application of a considerable amount of past study on crossed gratings to sampled gratings. However, this is not completely accurate. The two phenomena are fundamentally different, and it has never been shown explicitly how well crossed gratings can model the effects of a digital camera. The moire patterns which result from crossed gratings are due to the hetrodyning of their respective spatial frequencies. Moire patterns from digital cameras (or any periodic, discrete, sampling device) come from aliasing of the spatial frequencies of the

imaged grating. There have been moire pattern models which explicitly account for this discrete sampling, but they do not account for lens blur or multiple stages of sampling. In this paper, we present notationally consistent, frequency-space models of crossed-grating and sampled-grating moire from flat gratings. Our sampled-grating model is a new formulation which accounts for the video transmission (including lens blur) and multiple sampling stages in most digital imaging systems. We use our multiple stage sampling model to demonstrate how ignoring multiple sampling stages can lead to mistakes in moire analysis. We present results of an experiment which verifies the model used in the sampled-grating formulation. We also examine the ability of crossed gratings to model sampled gratings by developing a model of sampled-grating moire patterns using crossed gratings, and we verify the model qualitatively with a simple experiment.

2 A Model of Moire Patterns from Crossed Gratings

In this section we derive the Fourier transform of the superposition of an arbitrary number of flat, periodic, crossed gratings with arbitrary profiles. Gratings are usually considered as transparencies with regions of transmittance varying between zero and one. We can express the transmittance of any infinite, 2-D, periodic grating whose transmittance profile satisfies the Dirichlet conditions [Gas78] (p.108), and which is oriented so that its lines run perpendicular to the x axis, as the Fourier series

$$g(x,y) = \sum_{n=-\infty}^{\infty} c_n \exp(\frac{jn2\pi x}{T}), \tag{1}$$

where T is the period of the grating, and the c_n are the complex coefficients of the Fourier series of the 1-D transmission profile along the x axis. We note that any physically realizable transmittance grating will satisfy the Dirichlet conditions.

If the profile of the grating $g(x,y)$ is a square wave as shown in Figure 2, the c_n will be given by $c_n = h\,\mathrm{sinc}(nh)$, where $\mathrm{sinc}(x) = \sin(\pi x)/(\pi x)$, and h is the fraction of a period that is transparent. If $h = 1/2$, then the grating is called a Ronchi ruling, as shown in Figure 3.

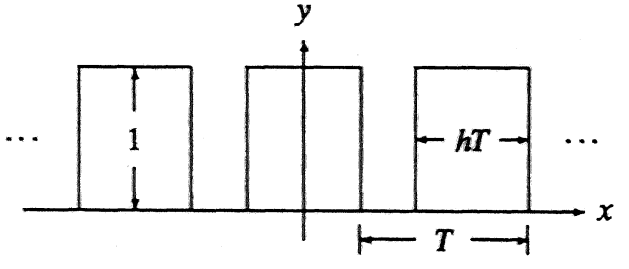

Figure 2: Square wave transmittance profile

The Fourier transform of $g(x,y)$ is

$$G(f_x,f_y) = \int_{-\infty}^{\infty}\int_{-\infty}^{\infty} g(x,y)\exp[-j2\pi(f_x x + f_y y)]dxdy.$$

The frequencies f_x and f_y are in units of cycles/unit length. We will use uppercase letters to indicate the Fourier transforms of corresponding lowercase, spatial functions. Substituting the Fourier series for the general grating $g(x, y)$ into the Fourier transform equation gives

$$G(f_x,f_y) = \sum_{n=-\infty}^{\infty} c_n \delta(f_x - \frac{n}{T},f_y).$$

This is a set of evenly spaced, Dirac δ-functions spread along the f_x axis. The volumes of the δ's are given by the Fourier series coefficients. Figure 4 shows a plot of the Fourier transform of the Ronchi ruling in Figure 3. The dots show the position of the δ-functions with the corresponding value of n above in parentheses. The area of a dot is proportional to the magnitude of its coefficient. For a Ronchi ruling, however, every δ with an even, nonzero n will have a coefficient of zero. We show these with small dots.

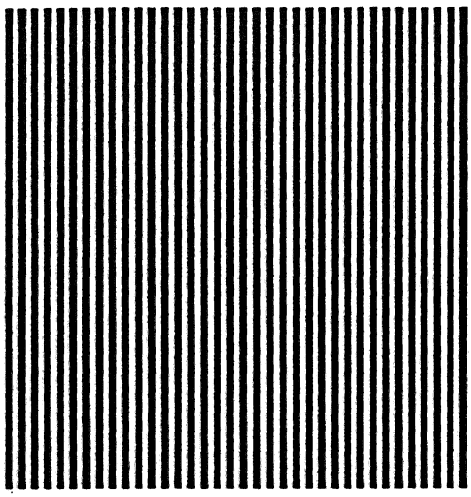

Figure 3: Ronchi ruling at 0°

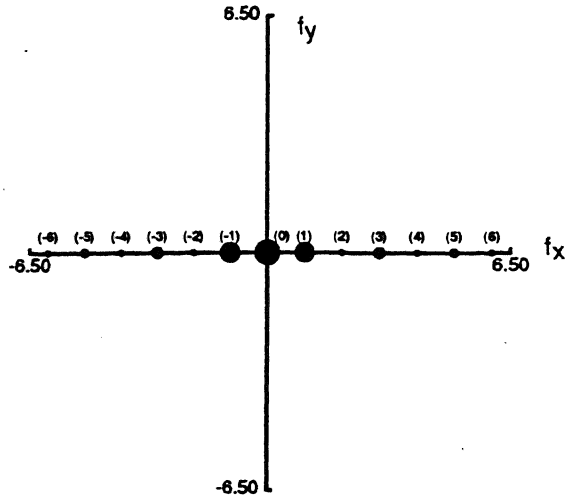

Figure 4: Fourier transform of Ronchi ruling at 0°

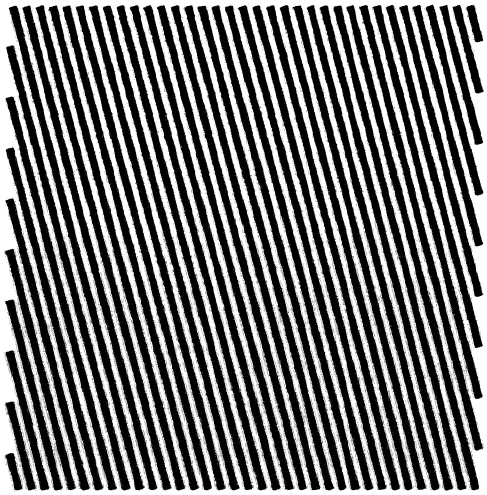

Figure 5: Ronchi ruling at 15°

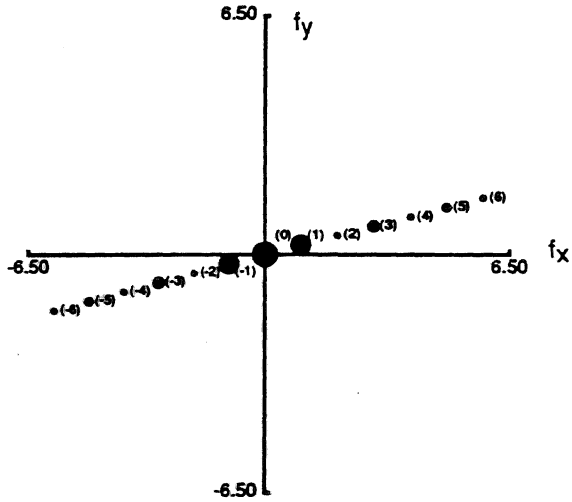

Figure 6: Fourier transform of Ronchi ruling at 15°

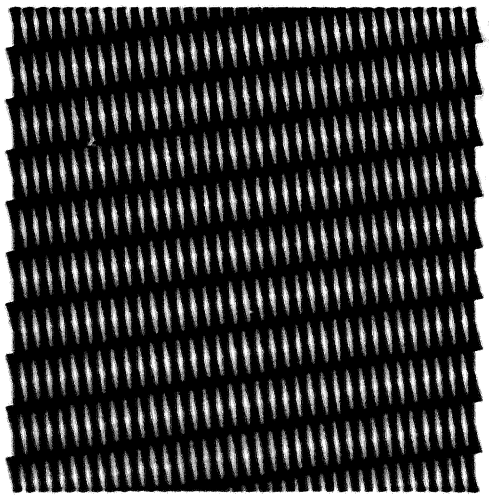

Figure 7: Crossed Ronchi rulings at 0° and 15°

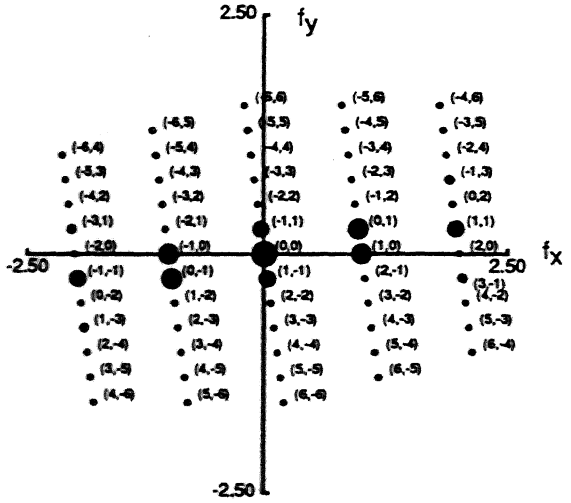

Figure 8: Fourier transform of crossed Ronchi rulings at 0° and 15°

We will call the orientation of $g(x,y)$ zero because the δ's of its Fourier transform occur along the f_x axis. If $g(x,y)$ is rotated around the origin by an angle θ, its Fourier transform rotates in exactly the same way. This is shown in Figures 5 and 6 where we show a Ronchi ruling rotated 15^o and its Fourier transform. The dots in Figure 6 are labeled like those in Figure 4. If $g_i(x,y)$ is a rotated version of $g(x,y)$, its Fourier transform is

$$G_i(f_x,f_y) = \sum_{n_i=-\infty}^{\infty} c_{n_i}\delta(f_x - \frac{n_i}{T_i}\cos\theta_i, f_y - \frac{n_i}{T_i}\sin\theta_i), \tag{2}$$

where we have begun subscripting with i to account for multiple gratings. Only the positions of the δ's change, not the coefficients.

If two of these transmittance gratings, $g_0(x,y)$ and $g_1(x,y)$, are superimposed, the resulting net transmittance will be given by the product of the constituent transmittances, $g_0(x,y)g_1(x,y)$. The Fourier transform of the net transmittance will be the 2-D convolution of the Fourier transforms, $G_0(f_x,f_y) * G_1(f_x,f_y)$.

We show the two Ronchi rulings of Figures 3 and 5 crossed in Figure 7. The Fourier transform of the crossed gratings is shown in Figure 8. We can think of the convolution operation graphically by considering the Fourier transforms in Figures 4 and 6 of the two constituent gratings. The first step in a 2-D convolution is to flip either one of the Fourier transforms around both the f_x and f_y axes. Since the Fourier transforms of the gratings as we have defined them are symmetric lines of δ's, this operation leaves the function unchanged. The next step is to record the value of the product of the two functions as a function of the offset of one of them. If we slide, say, the Fourier transform of the rotated grating around in (f_x,f_y) space over the Fourier transform of the unrotated grating, we see that the product will only be nonzero when two δ's overlap, at which point the product will the the product of the coefficients of the overlapping δ's. As the Fourier transform of the rotated grating is moved, the position of its center δ will indicate the value of the offset. Since two different lines cannot intersect at more than one point, it is clear that there will be, at most, only one pair of overlapping δ's for any given offset. Thus, we overlap every possible pair of δ's, recording the product of their coefficients at the position of the center peak of the sliding Fourier transform.

If $g_i(x,y)$ has period T_i, angle θ_i, and Fourier series coefficients c_{n_i}, then the Fourier transform of two superimposed gratings will be

$$G_0(f_x,f_y) * G_1(f_x,f_y) = \sum_{n_0=-\infty}^{\infty}\sum_{n_1=-\infty}^{\infty} c_{n_0}c_{n_1}\delta(f_x - \frac{n_0}{T_0}\cos\theta_0 - \frac{n_1}{T_1}\cos\theta_1, f_y - \frac{n_0}{T_0}\sin\theta_0 - \frac{n_1}{T_1}\sin\theta_1).$$

The parameters for the Ronchi rulings in the figures are $T_0 = T_1 = 1$, $\theta_0 = 0$, and $\theta_1 = 15^o$. The ordered pairs in the Fourier transform in Figure 8 show (n_0,n_1). In general, the locations of the δ's in frequency space are given by vectors

$$(f_x,f_y) = (\frac{n_0}{T_0}\cos\theta_0 + \frac{n_1}{T_1}\cos\theta_1, \frac{n_0}{T_0}\sin\theta_0 + \frac{n_1}{T_1}\sin\theta_1)$$

for $n_0, n_1 = -\infty,\ldots,-1,0,1,\ldots,\infty$. This vector interpretation was suggested by Bryngdahl [Bry74]. The amplitudes of the corresponding complex exponentials in the spatial domain are given by $c_{n_0}c_{n_1}$. A moire pattern is obvious when a δ with sufficient amplitude falls closer to the origin than the fundamental frequencies of either of the constituent gratings. In the case of Figure 8, the fundamental frequency of both gratings is 1 cycle/unit length. The lowest frequency shown in the Fourier tranform of the superimposed gratings is for $(n_0,n_1) = \pm(-1,1)$,

whose frequency is about ± 0.26 cycles/unit length in the direction of 97.5^o. These are the frequency and direction of the dark, nearly horizontal bands seen in the moire pattern in Figure 7.

For every relatively prime pair (n_0, n_1) in the Fourier transform of the superimposed gratings (Figure 8), there will be a set of δ's which fall on a line through the origin of frequency space, and whose n's are given by (mn_0, mn_1), $m = -\infty, \ldots, -1, 0, 1, \ldots, \infty$. These lines of δ's in frequency space form periodic patterns in the spatial domain, because their harmonics are spaced at equal intervals. The line of δ's whose relatively prime pair is $(n_0, n_1) = (-1, 1)$ in Figure 8 is responsible for the obvious moire pattern in Figure 7, because it happens to have a low fundamental frequency with a relatively large amplitude. There are, however, an infinite number of relatively prime pairs, all of which serve as the fundamental frequency of a line of δ's, all of which could be considered moire patterns. The well-known method of partial sum extraction [PYS76] is to pick a relatively prime pair and sum up all the frequencies along that line. Lines of δ's with higher fundamental frequencies are sometimes ignored as noise [PYS76].

If k transmittance gratings are superimposed, the above equation for the Fourier transform generalizes to

$$G_0(f_x,f_y) * G_1(f_x,f_y) * \ldots * G_{k-1}(f_x,f_y) = \sum_{n_0=-\infty}^{\infty} \sum_{n_1=-\infty}^{\infty} \cdots \sum_{n_{k-1}=-\infty}^{\infty} \left[\left(\prod_{i=0}^{k-1} c_{n_i} \right) \delta \left(f_x - \sum_{i=0}^{k-1} \frac{n_i}{T_i} \cos\theta_i, f_y - \sum_{i=0}^{k-1} \frac{n_i}{T_i} \sin\theta_i \right) \right] \quad (3)$$

This is a distribution of δ-functions at

$$(f_x,f_y) = \left(\sum_{i=0}^{k-1} \frac{n_i}{T_i} \cos\theta_i, \sum_{i=0}^{k-1} \frac{n_i}{T_i} \sin\theta_i \right)$$

with coefficients of $\prod_{i=0}^{k-1} c_{n_i}$.

3 Moire Patterns from Sampled Gratings

The previous section shows how moire patterns develop from crossed gratings. Digital cameras cause moire patterns by discrete sampling. The development of moire patterns in sampled images is fundamentally different from crossed gratings. Sampled-grating moire patterns occur when a periodic pattern is sampled at a rate less than twice the highest spatial frequency of the periodic pattern. This is the familiar phenomenon of aliasing. Spatial frequencies which are greater than half the Nyquist frequency are aliased into lower frequencies. Thus, much like the crossed-gratings case, high frequencies patterns beget patterns of lower frequencies.

At least two sampled-grating moire models have appeared in the literature. Bell and Koliopoulos [BK84] consider discrete, 2-D sampling of a projected, cosinusoidal grating and develop a rule for producing unambiguous moire fringes. Cetica *et al.* [CFB85] specialize Bell and Koliopoulos' result to one dimension and report an experiment with a linear, photodiode array. Neither model takes into account the effects of camera blurring or the multiple stages of sampling which are common in digital imaging systems. We will develop a model which accounts for these factors in the next section, and then apply it to a flat, periodic grating. It will be seen that blurring and multiple-stage sampling have a significant impact on the brightness and geometry of moire fringes.

3.1 A Model of Multiple Stage Reconstruction and Sampling

We will give a brief formulation of a single-stage, image sampling system to demonstrate aliasing. Similar formulations can be found in most texts on image processing. The model can be easily explained in terms of a digital camera recording an image, although we will see how the model can be applied, recursively, to subsequent stages of image transfer and display. The input to the sampling system is an arbitrary image of intensities $g(x,y)$. Before sampling, it is blurred by a convolution with the point spread function $p(x,y)$. For the case of a camera, $g(x,y)$ is the ideal input image, and $p(x,y)$ represents the effects of misfocus, diffraction, and pixel response, all of which can be described by convolution. (We are neglecting geometric and photometric scale factors here.) The image which is sampled by the photosensitive camera cells is then $p(x,y) * g(x,y)$. The Fourier transform of this image is $P(f_x,f_y)G(f_x,f_y)$, where $P(f_x,f_y)$ is the Fourier transform of the point spread function, and $G(f_x,f_y)$ is the Fourier transform of the ideal image. The camera's sampling grid can be represented by a grid of δ-functions, each centered on a photosensitive cell on the image plane. If the spacing of the cells in the x and y directions is T_x and T_y, the sampling grid is given by $\sum_{n_y=-\infty}^{\infty}\sum_{n_x=-\infty}^{\infty}\delta(x-n_xT_x, y-n_yT_y)$. Here we have neglected the finite size of the sampling array. This can be accounted for by multiplying the array by a zero-one function in the shape of the sampling grid (usually a rectangle). Bell and Koliopoulos do this in their analysis of moire patterns, but for our purposes, it only leads to unnecessary complications. This is because although a truncated sampling grid can have a significant impact on the frequency-domain representation of a sampled grating, it's spatial-domain representation (where moire pattern analysis is ultimately carried out) is simply a truncated version of the infinite moire pattern. The sampled image is given by the product of the blurred image and the sampling array as

$$[p(x,y) * g(x,y)] \sum_{n_x=-\infty}^{\infty}\sum_{n_y=-\infty}^{\infty}\delta(x-n_xT_x, y-n_yT_y).$$

The Fourier transform of this is the convolution of the Fourier transform of the blurred image and the Fourier transform of the sampling grid:

$$[P(f_x,f_y)G(f_x,f_y)] * \frac{1}{T_xT_y}\sum_{n_x=-\infty}^{\infty}\sum_{n_y=-\infty}^{\infty}\delta\left(f_x-\frac{n_x}{T_x}, f_y-\frac{n_y}{T_y}\right) . \quad (4)$$

This equation indicates that the Fourier transform of the blurred image is repeated at intervals of $(1/T_x, 1/T_y)$ in frequency space. These copies of the Fourier transform are called the *spectral orders* of the function $g(x,y)$, with the 0^{th} spectral order centered at the origin of frequency space.

Figure 9 shows the Fourier transform of a function $g(x,y)$ that is to be sampled. In this case, the function happens to be a grating. The δ-functions are shown as $\times$'s. After sampling, the Fourier transform looks like Figure 10. The original Fourier transform has been repeated into an infinite number of spectral orders. The 0^{th} spectral order is shown in $\times$'s, while the others are shown as $\bullet$'s. The centers of the spectral orders are shown with larger symbols.

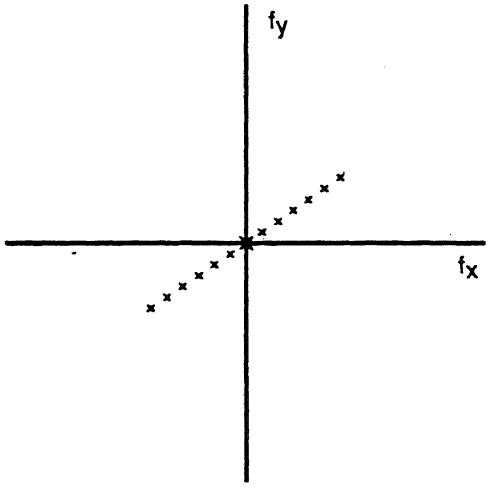

Figure 9: Fourier transform of grating

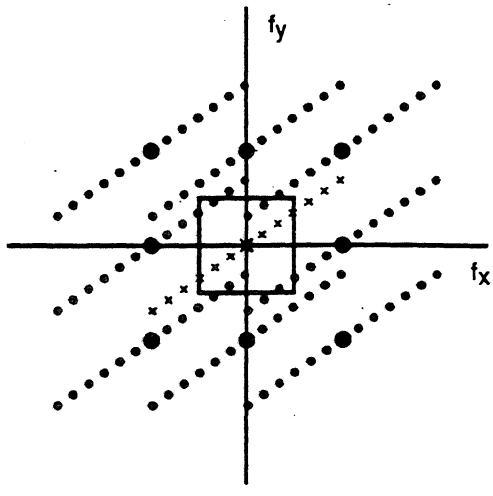

Figure 10: Spectral orders after first stage sampling

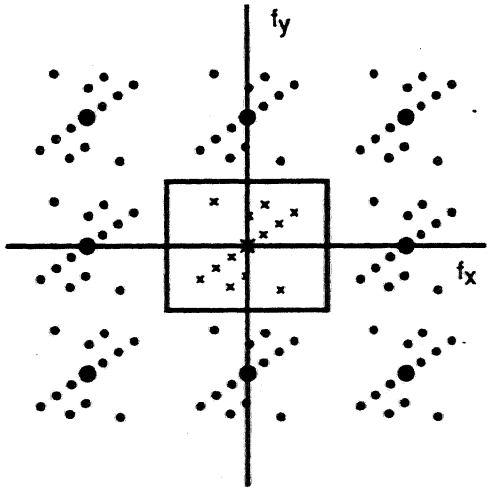

Figure 11: Spectral orders after second stage sampling, no additional aliasing

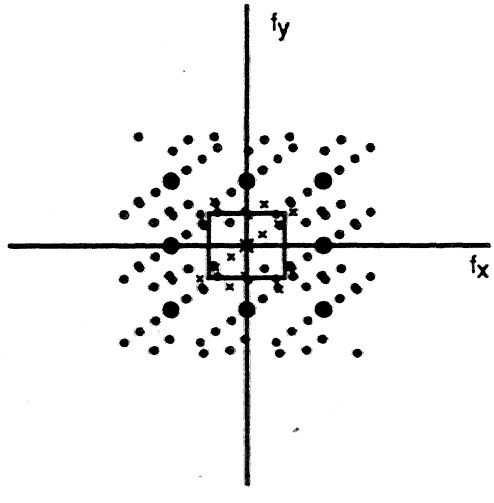

Figure 12: Spectral orders after second stage sampling showing additional aliasing

Interpolation is applied to the samples in order to extract a continuous estimate of the original image. This can be formulated in the spatial domain as a convolution of an interpolation function, usually some kind of narrow pulse, with the samples. The convolution operation means that the interpolation function is repeated at every sample point and modulated by the values of the discrete samples. In frequency space, interpolation amounts to multiplying the distribution of spectral orders by the Fourier transform of the interpolation function. This function may be chosen to reduce the effects of aliasing or noise, but it is always band-limited by the Nyquist frequencies, $[\pm 1/(2T_x), \pm 1/(2T_y)]$. These limits are shown as a rectangle in Figure 10. If frequencies from spectral orders other than the *0th* fall inside the nonzero region of the interpolation function, aliasing will occur. This has happened in Figure 10.

For a typical digital image capture and storage system, the model above is incomplete. Once the image is sampled into charge levels in the camera, the samples are converted into an analog, video signal for transmission, then amplified, filtered and resampled by an analog-to-digital converter. Thus, one set of samples is turned into another, and the sampling rates may not be equal. We show the frequency domain effects of a second stage of sampling in Figures 11 and 12.

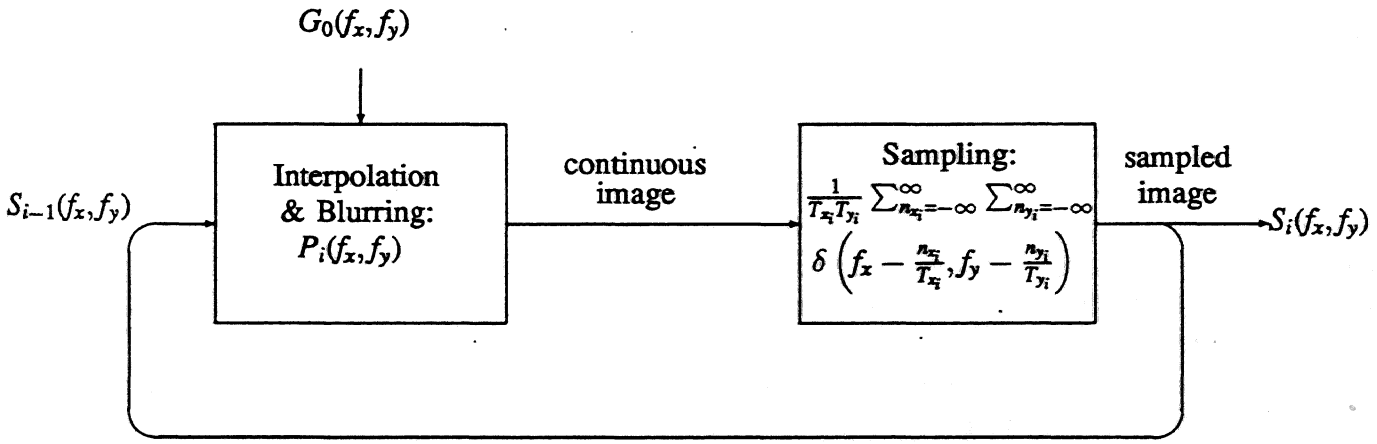

Figure 13: Block diagram illustrating multiple stage reconstruction and sampling

We can think of such a system as a multiple stage reconstruction and sampling process. As shown in Figure 13, each pass produces a new set of samples which are fed back through the system. The index i is incremented for each pass. The initial input to the system is the original, ideal image from the scene. It is first blurred and then sampled. The samples are then sent back through the system, where they are reconstructed into a continuous image and blurred (in the same step), and then sampled again. The process can be repeated over and over.

As we saw above, the reconstructed image is bandlimited by the Nyquist frequencies. Since a pass through the loop does not impose any higher frequencies on the reconstructed image, the final reconstructed image, no matter how many times the loop has been traversed, will be bandlimited by the minimum Nyquist frequency encountered during any pass. Thus, no aliasing can occur after the minimum sampling frequency has been encountered. Alternatively, if the sampling rate decreases on each pass, there may be a complex interaction of frequencies as aliased frequencies become themselves aliased in subsequent passes. These arguments apply independently to the x and y directions.

The process can be characterized mathematically by putting subscripts on equation 4, which describes one pass in the frequency domain.

$$S_i(f_x,f_y) = [P_i(f_x,f_y)S_{i-1}(f_x,f_y)] * \frac{1}{T_{x_i}T_{y_i}} \sum_{n_{x_i}=-\infty}^{\infty} \sum_{n_{y_i}=-\infty}^{\infty} \delta(f_x - \frac{n_{x_i}}{T_{x_i}}, f_y - \frac{n_{y_i}}{T_{y_i}}) \quad (5)$$

We have replaced G with S to stand for "samples". One pass may be interpreted as follows: The samples $S_{i-1}(f_x,f_y)$ are converted to a continuous signal by filtering with $P_i(f_x,f_y)$. P_i represents not only the interpolation function, but the amplification and filtering that occurs before the i^{th} sampling stage. The analog signal is then sampled with x and y spacings of T_{x_i} and T_{y_i}, giving a new set of samples in $S_i(f_x,f_y)$.

The process of creating a stored, digital image of a scene may be cast in this multiple stage model. We start with the ideal image $G(f_x,f_y)$ which serves as $S_0(f_x,f_y)$, the initial sampled image. While this is not really a sampled image, it is the appropriate place to start the recursion. The first sampling loop ($i = 1$) is the digital camera. $P_1(f_x,f_y)$ accounts for lens defocus, diffraction, and the area integration of the pixels which are spaced at intervals of T_{x_1} and T_{y_1}. The resulting samples are manifest as charges present on the image plane. The second sampling loop ($i = 2$) is the analog-to-digital conversion. This stage starts by converting the image plane charges to a 1-D analog signal using $P_2(f_x,f_y)$. Since the image plane samples are usually scanned out row by row, there is no blurring in the y direction in this step. For the same reason, $T_{y_2} = T_{y_1}$. T_{x_2} and T_{x_1} are not necessarily equal, because the sampling rate on the image plane may be different from the sampling rate of the digitizer. We could go around the loop once more to model the conversion to discrete charges on the phosphors of a display device. Yet another loop could model certain facets of human vision, since the discrete sampling of the human fovea can produce moire patterns, suggesting that it, too, has a fairly regular sampling grid (although not rectangular[Wil85]). This would require that the model accommodate a non-rectangular sampling grid.

The impossibility of aliasing after encountering the minimum sampling rate can be seen in Equation 5. Suppose that in pass $i = 1$ (*e.g.* the sampling on the camera's image plane), the sampling periods T_{x_1} and T_{y_1} are larger than the sampling periods of the digitizer, T_{x_2} and T_{y_2} in pass $i = 2$. That is, the sampling frequency of the first stage is lower than that of the second stage. The Fourier transform of the first set of samples will be a distribution of spectral orders at intervals of $(1/T_{x_1}, 1/T_{y_1})$. When this signal is reconstructed in preparation for resampling in the second stage, it will be bandlimited by the Nyquist frequencies of the first sampling stage, $[\pm 1/(2T_{x_1}), \pm 1/(2T_{y_1})]$. The Fourier transform of the second set of samples will again be a distribution of spectral orders, centered at intervals of $(1/T_{x_2}, 1/T_{y_2})$. Since these centers are farther apart than the maximum dimensions of the Fourier transform of the reconstructed image, there will be no overlap in frequencies, and thus no aliasing.

This is demonstrated graphically in Figures 10 and 11. The reconstructed image after one stage of sampling will consist of the δ's inside the Nyquist bounding box in Figure 10. These frequencies include some (but not all) of the frequencies of the original grating along with aliased frequencies from neighboring spectral orders. If this reconstructed image is sampled again with smaller sampling periods (*i.e.* higher sampling frequencies), the spectral orders of the sampled image will be spread in frequency space such that no overlap occurs, as in Figure 11. Here we have again shown the 0^{th} spectral order as $\times$'s and the others as $\bullet$'s. The box indicates the Nyquist bounds of the second sampling stage. If, on the other hand, the sampling rates of the second stage are lower than those of the first stage, more aliasing could occur. This is the case in

Figure 12. We see that the Nyquist bounding box includes some frequencies from neighboring spectral orders and excludes some from the 0^{th} order.

3.2 Moire Patterns

We can use the multiple stage sampling and reconstruction model above to predict the development of moire patterns in an image sampling system. Equation 5 gives the expression for one pass through the sampling system with an arbitrary input function $G(f_x,f_y)$. Equation 2 is a grating with an arbitrary profile at an angle θ. If we substitute the grating equation into the sampling equation, we see that the result of one stage of sampling on a rotated grating is

$$S_1(f_x,f_y) = \frac{1}{T_{x_1}T_{y_1}} \sum_{n_{y_1}=-\infty}^{\infty}\sum_{n_{x_1}=-\infty}^{\infty}\sum_{n_0=-\infty}^{\infty} c_{n_0}P_1\left(\frac{n_0}{T_0}\cos\theta_0, \frac{n_0}{T_0}\sin\theta_0\right)\delta\left(f_x - \frac{n_0}{T_0}\cos\theta_0 - \frac{n_{x_1}}{T_{x_1}}, f_y - \frac{n_0}{T_0}\sin\theta_0 - \frac{n_{y_1}}{T_{y_1}}\right) \quad (6)$$

This is a distribution of δ's whose locations are given by

$$(f_x,f_y) = \left(\frac{n_0}{T_0}\cos\theta_0 + \frac{n_{x_1}}{T_{x_1}}, \frac{n_0}{T_0}\sin\theta_0 - \frac{n_{y_1}}{T_{y_1}}\right).$$

The δ's of the grating's Fourier transform are indexed by n_0, while the spectral orders are indexed by (n_{x_1}, n_{y_1}). The coefficients of the δ-functions are independent of the particular spectral order, but depend on the relative displacement from the center of the spectral order. As with crossed gratings, a moire pattern will be especially obvious if the first fundamental frequency from another spectral order falls closer to the origin than the fundamental frequency of the $0th$ spectral order, because the first fundamental usually has significant amplitude. See [RK82] (pp. 83-87) for a simple example.

In most digital imaging systems, the image above will be reconstructed and sampled again. This process can have a significant effect on the moire patterns which are observed in the final image. Given a suitable set of geometric parameters (*i.e.* the rotation of the grating and the sampling intervals), there could actually be moire patterns developed in the first stage that are aliased into other moire patterns in subsequent stages. This was shown in Figures 10 and 12 where frequencies which were aliased in the first sampling stage were again aliased in the second stage. These extra, aliased frequencies cannot be accounted for in a single-stage sampling model, and they would likely confound current moire fringe analysis techniques.

In addition to affecting the geometry of moire fringes, multiple sampling stages also affect their brightness. Each sampling stage has associated with it its own point spread function which describes the combined effects of interpolated reconstruction and transmission to the next sampling stage. Mathematically, the applications of the sampling grids and point spread functions must be interleaved, which means that, in general, no single point spread function can be used to characterize multiple sampling stages. Previous models of sampled-grating moire have used either a simple, single-stage model with only one point spread function, or else no point spread function at all. As was shown in Post's [Pos67] work on fringe sharpening, a careful analysis of the brightness profiles of moire fringes can lead to more robust detection of the fringes. Thus, it is important to have an accurate model of the sampling system's effect on the fringe profiles.

4 Crossed-Gratings Models of Sampled Gratings

Equation 3, which describes crossed-grating moire, and Equation 6, which describes sampled-grating moire, are surprisingly similar, given the fundamentally different processes which they model. They are both a regularly-spaced distribution of δ-functions. It has been asserted that the moire patterns which result from digitally sampling gratings and those from crossed gratings can be considered equivalent [IYS77]. The intuitive feeling behind this assertion is that the rows and columns of the sampling grid can be considered as gratings which, when combined with an object grating, make moire patterns like crossed gratings. This is important because it means that the considerable amount of past work on metrology using crossed-grating moire can be directly applied to the relatively new idea of "scanning moire" — moire with one grating and a digital camera.

In order to assess the degree of similarity between crossed gratings and sampled gratings, we will try to model a sampled grating with crossed gratings. We imagine a single grating $g_0(x, y)$ (the object grating) which is imaged by a digital camera. The grating has period T_0, angle θ_0, and Fourier series coefficients c_{n_0}. If aliasing occurs, moire patterns will result in the reconstructed image. We would like to know what set of crossed gratings of the form of Equation 2 would give the same moire pattern for the same object grating. These "effective" gratings will be chosen such that they give approximately the same Fourier transform as the Fourier transform of the sampled, reconstructed image of grating $g_0(x, y)$. The effective gratings will serve as a sort of camera model. It is important to realize that the camera model is made of *gratings* (patterns of some transmission profile which is periodic along some direction), not arbitrary transmission functions. If we allowed arbitrary functions, then the camera model would be a simple inverse Fourier transform. We are restricting ourselves to gratings in order to test the assertion that sampled-grating moire patterns can be considered the same as crossed gratings. In addition, we will only attempt to model 1 1/2 passes through our multiple stage model, meaning that the input grating is first blurred, sampled, and then reconstructed. This is necessary because crossed gratings result in a continuous image, not a sampled image which results from one pass through the loop. A reconstructed, sampled image of a grating is given by

$$\frac{1}{T_{x_1} T_{y_1}} P_2(f_x, f_y) \left[\sum_{n_{y_1}=-\infty}^{\infty} \sum_{n_{x_1}=-\infty}^{\infty} \sum_{n_0=-\infty}^{\infty} c_{n_0} P_1\left(\frac{n_0}{T_0}\cos\theta_0, \frac{n_0}{T_0} sin\theta_0\right) \delta\left(f_x - \frac{n_0}{T_0}\cos\theta_0 - \frac{n_{x_1}}{T_{x_1}}, f_y - \frac{n_0}{T_0}\sin\theta_0 - \frac{n_{y_1}}{T_{y_1}}\right) \right] \tag{7}$$

Here P_1 is the Fourier transform of the point spread function of the camera (including lens and pixel shape), and P_2 represents the interpolation function.

The set of effective gratings is not unique. In fact, even the *number* of effective gratings is not determined. (For instance, any grating can be composed of two or more parallel gratings, each of which makes up part of the first grating's profile.) It is reasonable, however, to consider a set of two effective gratings, representing the rows and columns of the sampling grid respectively. We will first derive an approximate pair of effective gratings by assuming that they are each Ronchi rulings. We will then relax the conditions on the two effective gratings by allowing arbitrary profiles.

Our strategy in both cases will be to compare an equation which characterizes the assumed form of the effective gratings to Equation 7 which gives the moire patterns from a digital sampling system. We will then instantiate the free parameters of the effective gratings and evaluate how well the two equations match.

4.1 An Approximation With Two Ronchi Rulings

Equation 3 gives the expression for k superimposed, transmission gratings. We will let $k = 3$ for two effective gratings and one, arbitrary, object grating. The c_n for a Ronchi ruling are $\mathrm{sinc}(n/2)/2$. The expression for the superposition of the arbitrary grating $G_0(f_x,f_y)$ and the two Ronchi rulings representing the camera is then

$$\frac{1}{4}\sum_{n_0=-\infty}^{\infty}\sum_{n_1=-\infty}^{\infty}\sum_{n_2=-\infty}^{\infty} c_{n_0}\mathrm{sinc}(\frac{n_1}{2})\mathrm{sinc}(\frac{n_2}{2}) \quad \delta(f_x - \frac{n_0}{T_0}\cos\theta_0 - \frac{n_1}{T_1}\cos\theta_1 - \frac{n_2}{T_2}\cos\theta_2, \; f_y - \frac{n_0}{T_0}\sin\theta_0 - \frac{n_1}{T_1}\sin\theta_1 - \frac{n_2}{T_2}\sin\theta_2)$$

where T_0, θ_0, and c_{n_0} characterize the arbitrary grating. The free parameters are the periods and angles of the Ronchi rulings, *i.e.* T_1,T_2,θ_1, and θ_2. We see from Equation 7, which gives the expression for the sampled grating G_0, that a reasonable choice is to have $T_1 = T_x$, $T_2 = T_y$, $\theta_1 = 0$, and $\theta_2 = \frac{\pi}{2}$. The periods and angles of the effective gratings then match the periods and angles of the rows and columns of the sampling grid. The *positions* of the δ-functions in both the sampled-grating case and crossed-gratings case are thus equivalent. The amplitudes, however, are not. The most significant difference is that the sampled grating is bandlimited by the Nyquist frequencies, while the crossed gratings have no such limits. Likewise, the crossed gratings are not subject to the interpolation function or camera blur. Thus, two Ronchi rulings can accurately generate a superset of the frequencies from an aliased grating, but they will not give a good indication of the amplitudes.

We can demonstrate the Ronchi ruling approximation in pictures. Figure 3 and Figure 14 show the two constituent, orthogonal Ronchi rulings which serve to simulate the sampling grid of a camera. Figures 4 and 15 show the respective Fourier transforms. When these two gratings are crossed, they look like Figure 16, and the Fourier transform looks like Figure 17. The Fourier transform is a grid of δ's whose spacing is the reciprocal of the periods of the two Ronchi rulings. If the grating periods are equal to the sampling periods of the camera, as we have shown they should be, then the δ's of the two, orthogonal Ronchi rulings will coincide with the centers of the spectral orders of a sampled grating. In Figure 18 we show the two, orthogonal Ronchi rulings crossed with a third Ronchi ruling at 15°. This is the same 15° Ronchi ruling shown with its Fourier transform in Figures 5 and 6. Finally, Figure 19 shows the Fourier transform of the three, crossed Ronchi rulings. Although it is difficult to tell from the figure, the effect of convolving the Fourier transform of the tilted ruling with that of the two, orthogonal rulings has been to repeat the Fourier transform of the tilted ruling on a grid of δ's, just like the repeated spectral orders of a sampled grating.

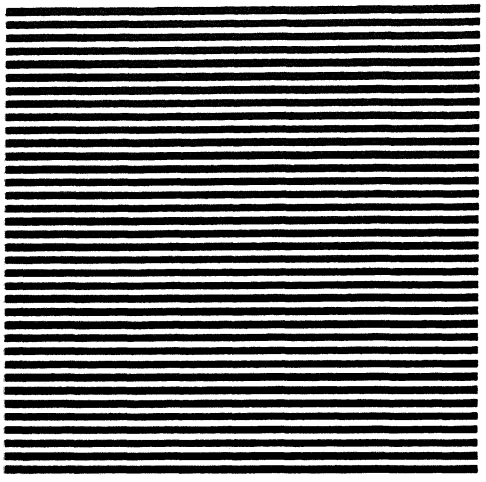

Figure 14: Ronchi Ruling at 90°

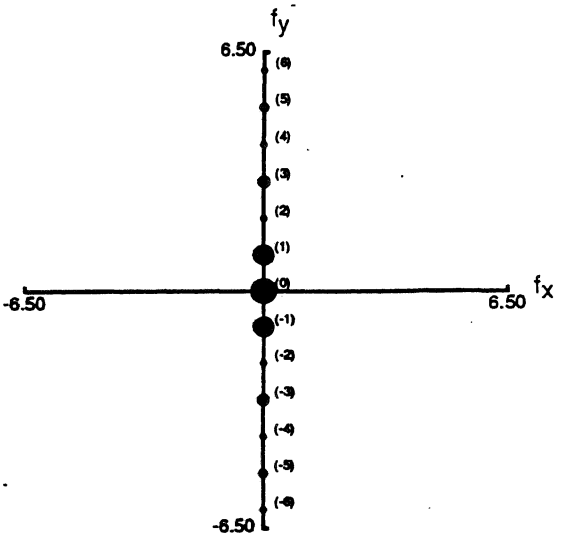

Figure 15: Fourier transform of Ronchi ruling at 90°

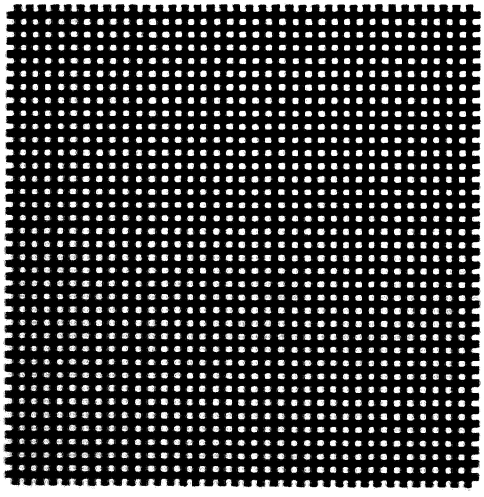

Figure 16: Crossed Ronchi rulings at 0° and 90°

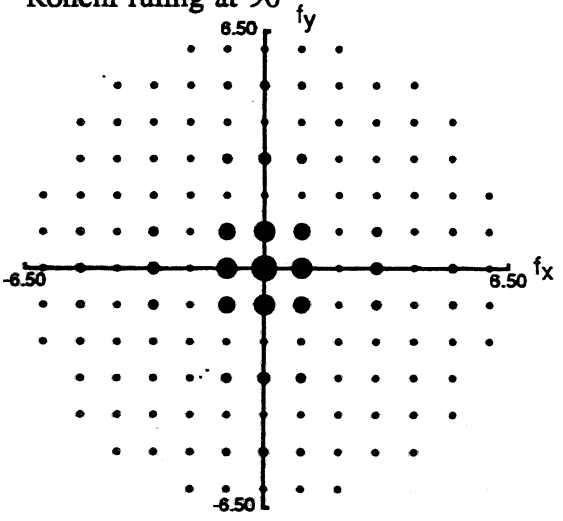

Figure 17: Fourier transform of crossed Ronchi rulings at 0° and 90°

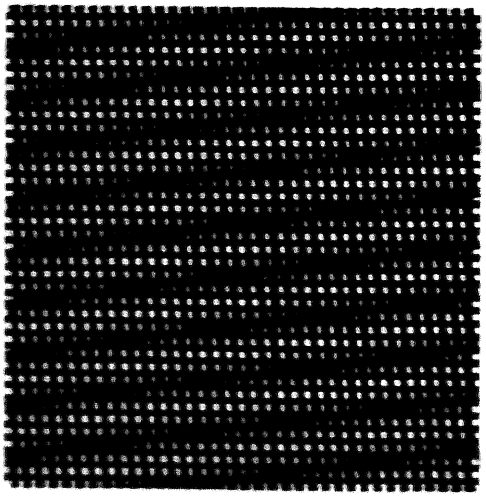

Figure 18: Crossed Ronchi rulings at 0°, 90° and 15°

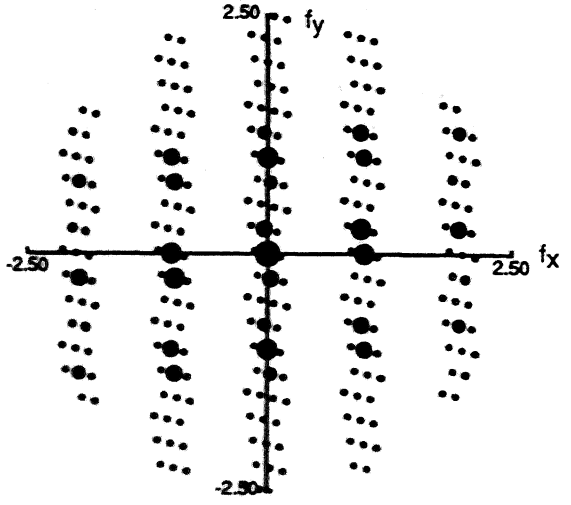

Figure 19: Fourier transform of crossed Ronchi rulings at 0°, 90° and 15°

4.2 An Approximation With Two Arbitrary Gratings

When we relax the conditions on the profiles of the two effective gratings, we still find that the geometric parameters should match those of the sampling grid. Thus, the equation for the crossed-gratings moire pattern becomes

$$\sum_{n_0=-\infty}^{\infty}\sum_{n_1=-\infty}^{\infty}\sum_{n_2=-\infty}^{\infty} c_{n_0}c_{n_1}c_{n_2}\delta(f_x - \frac{n_0}{T_0}\cos\theta_0 - \frac{n_1}{T_1}, f_y - \frac{n_0}{T_0}\sin\theta_0 - \frac{n_2}{T_2}) \tag{8}$$

Here again the positions of the δ-functions in both the crossed-gratings case and the aliased-grating case are equivalent. The remaining free parameters are the Fourier series coefficients, c_{n_1} and c_{n_2}, of the two effective gratings. We would like these coefficients to account for the point spread function of the camera and the interpolation function of the reconstruction. We see, however, that this is in general impossible, because these coefficients are not sensitive to the necessary variables. From Equation 7, the Fourier transform of the point spread function appears as $P_1(n_0\cos(\theta_0)/T_0, n_0 sin(\theta_0)/T_0)$. P_1 is a function of n_0, while c_{n_1} and c_{n_2} have no such dependence. Since the n's vary independently of each other in the three sums, $c_{n_1}c_{n_2}$ cannot, in general, be equal to $P_1(n_0\cos(\theta_0)/T_0, n_0 sin(\theta_0)/T_0)$. A similar argument applies to the interpolation function $P_2(f_x, f_y)$ which must be zero outside the Nyquist frequencies. For a given n_1 and n_2, the $c_{n_1}c_{n_2}$ product will multiply δ-functions at frequencies both inside and outside the the Nyquist bounds, because n_0 is still free to vary and take the δ-functions inside and outside the Nyquist bounds. Thus, by relaxing the conditions on the profiles, we cannot generally get better results than from the two Ronchi rulings.

We can reach a more concrete conclusion if we disregard the point spread function and the interpolation function for the sampled grating case (by setting them to one). By comparing Equations 7 and 8 we then have, for the effective gratings, $c_{n_1}c_{n_2} = 1/(T_xT_y)$. We will arbitrarily set $c_{n_1} = 1/T_x$ and $c_{n_2} = 1/T_y$. The Fourier series for $g_1(x,y)$, the effective grating with the vertical lines, becomes

$$\begin{aligned} g_1(x,y) &= \frac{1}{T_x}\sum_{n_1=-\infty}^{\infty} e^{\frac{in2\pi x}{T_0}} \\ &= \sum_{n_1=-\infty}^{\infty}\delta(x - n_1T_x). \end{aligned}$$

Similarly,

$$g_2(x,y) = \sum_{n_2=-\infty}^{\infty}\delta(y - n_2T_y).$$

These are each a series of evenly-spaced lines on otherwise opaque transparencies. Their product is a grid of pinholes, coincident with the centers of the pixels of the camera's image plane. These effective gratings model a camera with no blur and no Nyquist limitations.

The practical conclusion from these two-grating approximations is that the point spread function and interpolation function cannot be accurately modeled using crossed gratings, while the constituent frequencies can be. Thus, the body of research developed for crossed-grating moire can be applied to sampled-grating moire if the profiles of the moire patterns are not important. It should be noted that the crossed-gratings model predicts frequencies beyond the Nyquist bounds which will never appear in sampled-grating moire.

If we want to simulate more passes through the sampling and reconstruction loop, we can add two more gratings for each pass. The periods of the gratings should be equal to the sampling periods. Their angles should match the angles of the sampling grid. In this way, we can generate a superset of the constituent sinusoids of the sampled moire pattern, although the amplitudes will still not match.

5 Experimental Verification of Sampled-Grating Moire

We performed an experiment to verify our model of sampled-grating moire patterns by taking a digital image of a square-wave grating. We used a Sony CCD, monochrome camera, model AVC-D1, a Cosmicar 12.5 mm – 75 mm zoom lens, model number 24789, and an infrared filter under incandescent lights. The Sony is a conventional, medium quality camera purchased new in 1985. We created a square-wave grating using a 2-D graphics program and printed it on 28 cm $\times$ 43 cm paper using a laser printer. The period of the grating was about 0.85 mm, and the duty ratio h was about 0.48. The grating contained 301 lines. We sandwiched the grating in between a clear, plastic plate and a flat grid of calibration squares to reduce wrinkles in the grating, as shown in Figure 20. We registered the bottom of the grating with one of the horizontal lines on the calibration grid. The camera was positioned about 1 m away from the grating with its optical axis approximately normal to the the plane of the grating.

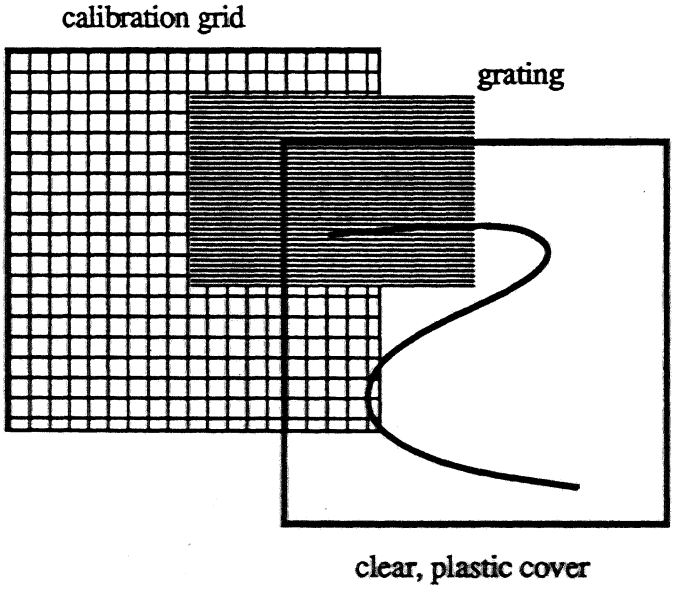

Figure 20: Method of mounting grating for experiment

The sampled-grating model predicts that the moire pattern will vary with the period and angle of the grating and the sampling periods of the camera. We could vary these values by adjusting the angle of the grating and the focal length of the lens. Indeed, the moire patterns varied wildly with only small adjustments.

Our 256 x 256 test image is shown in Figure 21, which can be compared to our simulated moire pattern in Figure 22. The dark, nearly horizontal bands make up the primary moire pattern. The lines of the grating are not visible because their fundamental spatial frequency was beyond

the Nyquist limits. There are still some wrinkles in the left half of the grating. The DFT of the actual moire pattern is shown in Figure 23. We have thresholded the DFT so the smaller peaks are still visible. The peaks are blurred because the DFT was taken over only a finite region of 2-D space.

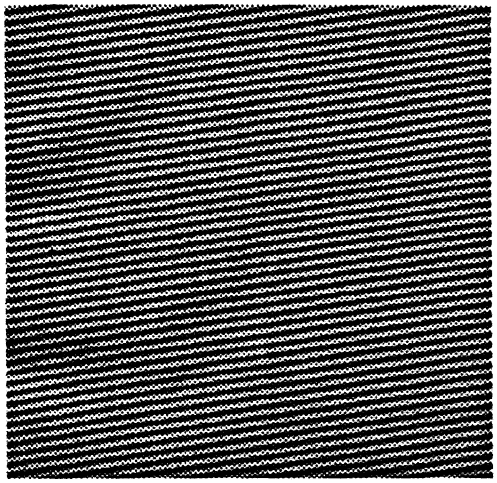

Figure 21: Sampled-Grating Moire Pattern

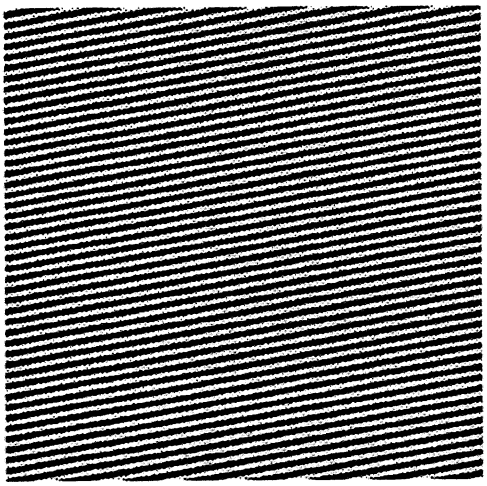

Figure 22: Predicted Moire Pattern

5.1 Geometric Parameters

In this section we describe how we determined the geometric parameters of the experiment and how well our model predicts the constituent frequencies of the moire pattern. We will take as our fundamental unit of length the "y-pixel". This is the sampling period of the CCD in the y-direction. Since the image is scanned out in rows, it is also the sampling period of the digitizer in the y-direction. We estimated the period and angle of the grating by slipping out the grating from in front of the calibration grid and taking another image. The calibration grid provided an absolute ground truth for scaling and rotation. Because of our choice of units, the sampling periods in the y-direction for the camera and digitizer were both one. We calculated the sampling rates in the x-direction from the specifications of the camera and digitizer. In terms of our multiple stage sampling model, we will call the camera "stage 1" and the digitizer "stage 2". The geometric parameters for our model were

$T_0 = 1.21$ y-pixels	$\theta_0 = 88.38^o$
$T_{x_1} = 1.70$ y-pixels	$T_{y_1} = 1.00$ y-pixels
$T_{x_2} = 1.28$ y-pixels	$T_{y_2} = 1.00$ y-pixels

.

The digitizer does not figure prominently in our predictions, because its two sampling rates, T_{x_2} and T_{y_2}, are both less than or equal to their respective counterparts on the CCD, T_{x_1} and T_{y_1}. As we saw previously, this means that no additional aliasing can occur in the digitization stage. Thus, the digitizer values represent true (unaliased) samples of the moire pattern after 1 1/2 passes through the reconstruction and sampling loop. Therefore, an adequate model of the process is Equation 7 which represents 1 1/2 passes. We note that this includes the effects of image blurring before sampling, CCD sampling, and any filtering which occurred before the image was digitized.

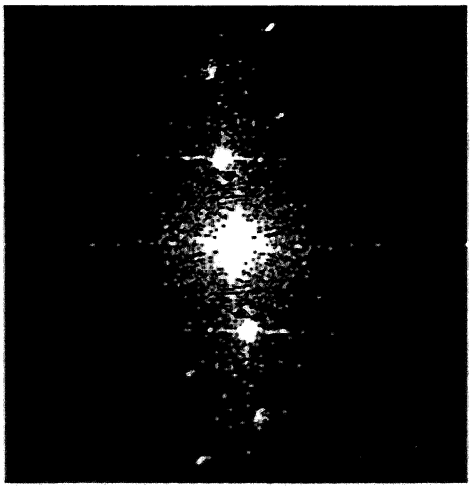

Figure 23: Thresholded Fourier Transform of Moire Pattern

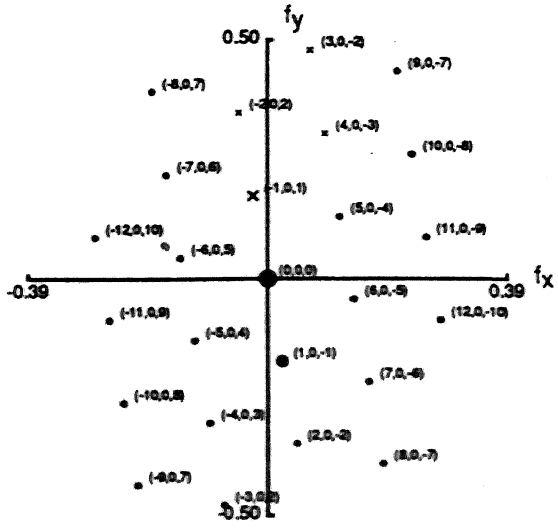

Figure 24: Predicted Fourier Transform of Moire Pattern

peak			prediction		experiment		error	
n_0	n_x	n_y	frequency ($\frac{\text{cycles}}{\text{y-pixel}}$)	angle	frequency ($\frac{\text{cycles}}{\text{y-pixel}}$)	angle	frequency	angle
-1	0	1	0.18	97.65^o	0.18	96.78^o	-3.04%	0.87^o
4	0	-3	0.32	72.94^o	0.28	74.20^o	13.70%	-1.26^o
-2	0	2	0.35	97.65^o	0.37	96.23^o	-3.98%	1.42^o
3	0	-2	0.48	81.66^o	0.46	82.71^o	5.83%	-1.04^o

Table 1: Predicted and actual frequencies of four peaks

A plot of the predicted Fourier transform is shown in Figure 24. The strongest, nonzero frequency on the plot is for $(n_0, n_x, n_y) = \pm(-1, 0, 1)$. These are the fundamental harmonics of the spectral orders just above and below the 0^{th} spectral order in frequency space. They have spilled into the region which is not cut off by the Nyquist bounds. In fact, the fundamental frequencies of the 0^{th} spectral order are outside the Nyquist bounds, so the grating itself is not visible in the image. The frequency of these strongest peaks is

$$(f_x, f_y) = (\frac{n_x}{T_{x_1}} + \frac{n_0}{T_0}\cos\theta_0, \frac{n_y}{T_{y_1}} + \frac{n_0}{T_0}\sin\theta_0) = \pm(-0.023, 0.17)\frac{\text{cycles}}{\text{y} - \text{pixel}}.$$

These two peaks sum to a cosine wave with a frequency of 0.18 cycles/y-pixel in a direction of 97.65^o from the horizontal. This is the obvious moire pattern that is apparent in Figure 21. An analysis of the DFT of the actual moire pattern shows the strongest, nonzero-frequency peak to be at a frequency of 0.18 cycles/y-pixel in a direction of 96.78^o, which is in good agreement with the predicted fundamental. We can visually match three other peaks between the actual and predicted Fourier transforms. The four matched peaks are shown as $\times$'s in Figure 24. The four actual and predicted values are given in Table 5.1. We note that the absolute value of the percentage error in frequency increases with increasing values of n_0 and n_y. This is because increasing these values magnifies the effect of errors in the geometric parameters T_0, θ_0, and T_y.

All the δ-functions on the plot in Figure 24 have $n_x = 0$. Since T_{x_1} appears only as n_x/T_{x_1} in the equation for the position of the δ's, the CCD sampling period in the x-direction has no effect on the moire patterns. This is because the grating was oriented so its lines were almost parallel to the rows of the CCD. If the grating were rotated through another 90^o, we would see the dependence on T_{y_1} lessen until all the $n_y = 0$. We suspect that Idesawa *et al.* [IYS77] had a similar situation, since they actually consider the camera to be modeled by one grating corresponding to the horizontal scanning lines of the camera.

5.2 Amplitude Prediction

Having successfully predicted the constituent frequencies of a sampled-grating moire pattern, we turn our attention to predicting the amplitudes of the sinusoids. The amplitude of a sinusoid (*i.e.* the coefficient of a δ-function in frequency space) is determined by three factors: the c_{n_0}, $P_1(f_x, f_y)$, and $P_2(f_x, f_y)$. The c_{n_0} are the Fourier series coefficients of the grating profile. We know these with a fair amount of confidence since we know that the profile is approximately a square wave with a duty ratio of about 0.48. Thus, $c_{n_0} = 0.48\text{sinc}(0.48n_0)$.

Finding P_1 and P_2 is more difficult. P_1 represents the effects of lens blur, diffraction, and the response of a single, photosensitive CCD element. P_2 represents the filtering which occurs in the electronics of the camera (when the CCD samples are being assembled into a 1-D, analog signal), the transmission from the camera to the digitizer, and the time sampling window of the digitizer for each digitized sample.

The CCD charge values are samples of P_1G, where G is the ideal input image. If P_1G is bandlimited below the Nyquist frequencies of the CCD, then no aliasing will occur in the camera sampling stage. The signal arriving at the digitizer sampling stage will then be P_1P_2G. If the digitization rate is sufficiently high (as it is in our case), then no additional aliasing will occur at this stage. In general, once the minimum x and y sampling rates have both been reached in a multiple stage sampling system, the transfer functions of successive steps will simply multiply into one effective transfer function. These are the (often tacit) band-limitation assumptions made by researchers when they attempt to measure the point spread function of a digital camera system by imaging a scene with high spatial frequencies such as a point, line, or step edge. Even if we did know the product P_1P_2, it would not be sufficient for our model. P_1 must be applied to the unaliased frequencies, while P_2 is applied after aliasing.

Ideally, we could determine P_2 by applying test charges to the CCD elements of our camera. Instead, we attempted to project a step edge onto the CCD by placing a piece of metal foil as close as we dared to the sampling chip. We were able to lay the foil on a glass cover over the chip, leaving about a 2mm gap of glass and gas between the two. The results were disappointing. The derived line-spread function varied significantly depending on whether the step edge was a dark-to-light or light-to-dark transition, and the crude transfer function that we derived from the data did not fit the moire pattern data well. We attribute this to many things. The step edge was subject to a certain amount of diffraction as its image traversed the gap, so we were not imaging a perfect step edge. There may have been aliasing in the higher harmonics of the step edge. Finally, we know that the camera electronics is not a purely linear system. For the rest of our experiment, we assumed that $P_2(f_x, f_y) = \text{rect}(T_x f_x, T_y f_y)$, that is, the only band limitations between the CCD and the digitizer were the Nyquist frequencies of the CCD. Given the difficulty of experimentally finding P_2, along with the acceptable predictions we were able to make in the end, we felt this to be a tolerable assumption.

Having accounted for two of the three amplitude attenuation factors (the c_{n_0} and P_2), we then attributed the remainder of the attenuation to P_1, which represents the effects of lens blur, diffraction, and the response of the CCD elements.

We can extract experimental data with which to fit this function from the actual moire pattern data in the form of the amplitudes of the four matched peaks from the previous section. Since P_1 is a function of the *pre-aliased* spatial frequencies, it is important to know what these frequencies were. From the peak matches in the previous section, we know the corresponding values of n_0 (the harmonics of the grating). The spatial frequency is then, from the Fourier series in Equation 1, n_0/T_0, where T_0 is the period of the grating. Since we measure T_0 in units of y-pixels, the spatial frequencies will be in units of cycles/y-pixel, consistent with the frequency units used above. The experimental magnitudes of the four matched frequencies come from the Fourier transform of the moire pattern. For each peak, we divided out the effects of P_2 (which we have assumed to be one inside the Nyquist bounds) and c_{n_0} to get the data with which to fit P_1.

In choosing the form of P_1, we decided to ignore the effects of lens blur and the CCD element response profile. We neglected lens blur because we focused very carefully with the aid

of a test pattern, and because we were imaging a flat scene perpendicular to the optical axis, so depth of field was not an important issue. We ignored the CCD element response because we did not have a good idea of the response profile. At one point we assumed a flat rectangular response, but it did not help the fit over accounting for diffraction alone.

We chose as the basis for P_2 the optical transfer function (OTF) derived by Goodman[Goo68] which describes the effects of diffraction of monochromatic, incoherent light in an aberration-free lens system with a circular exit pupil. It is

$$H(f,\lambda) = \begin{cases} \frac{2}{\pi}\left[\cos^{-1}\left(\frac{f}{2f_0}\right) - \frac{f}{2f_0}\sqrt{1-\left(\frac{f}{2f_0}\right)^2}\right] & \text{for } f \le 2f_0 \\ 0 & \text{otherwise} \end{cases}$$

It is a circularly symmetric function of spatial frequency f, so $f = \sqrt{f_x^2 + f_y^2}$. A plot of $H(f,\lambda)$ for two different wavelengths of light is shown in Figure 25. By convention, H is scaled so that $H(0,\lambda) = 1$. The value of f_0 is the spatial cutoff frequency of the corresponding coherent system, given by

$$f_0 = \frac{l}{2\lambda d},$$

where l is the diameter of the exit pupil of the lens, d is the distance from the last lens to the image plane, and λ is the wavelength of the monochromatic light. For our purposes, it is sufficient to consider the ratio l/d as a single parameter of the lens system.

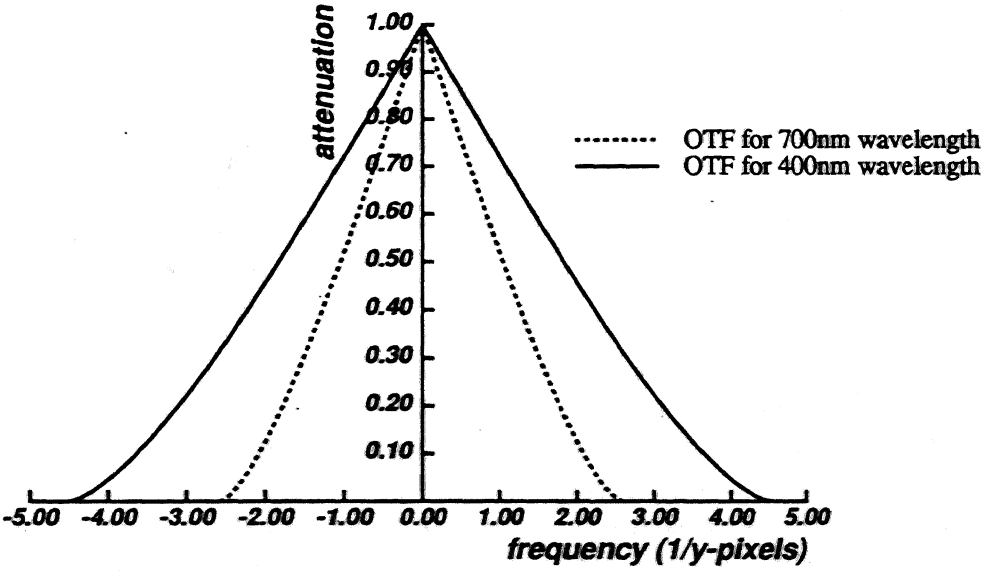

Figure 25: OTF's for monochromatic, incoherent light

If the spectrum of incident light were narrow enough, it would be sufficient to use $H(f,\lambda)$ directly. But, as can be seen in Figure 25, there is a significant difference in H from one side of the visible spectrum to the other. The effects of polychromatic light can be taken into account by using a sum of $H(f,\lambda)$ weighted by the power of the incident light at every wavelength. The effect is to integrate out the wavelength variable. If the power spectrum of the incident, incoherent light is $s(\lambda)$, then the polychromatic OTF is given by

$$P_1(f) = \frac{\int_0^\infty s(\lambda)H(f,\lambda)d\lambda}{\int_0^\infty s(\lambda)H(0,\lambda)d\lambda}$$

where we have normalized so $P_1(0) = 1$.

The power spectrum of the light, which orginated from an incandescent bulb, was affected by the reflection from the grating and by the passage through the camera lens and filter. In addition, the CCD has a particular spectral response profile. We approximated the spectrum of the incandescent bulb with CIE Standard Illuminant A, which was appropriate because it models idealized incandescent bulbs. We assumed that the grating (and plastic cover) had a flat spectral response based on the simple observation that it looked white to our eyes. Since the rest of the system was bandlimited to the visible spectrum, this assumption was appropriate. The response of the filter, lens, and CCD were taken from spectroradiometer measurements in our laboratory. The constituent and resulting spectra are shown in Figure 26. We have scaled all the spectra so their maxima are one. The curve we used for $s(\lambda)$ is the product of the curves for the illuminant, infrared filter, and the combined lens and CCD response. It is shown as a solid line in the figure.

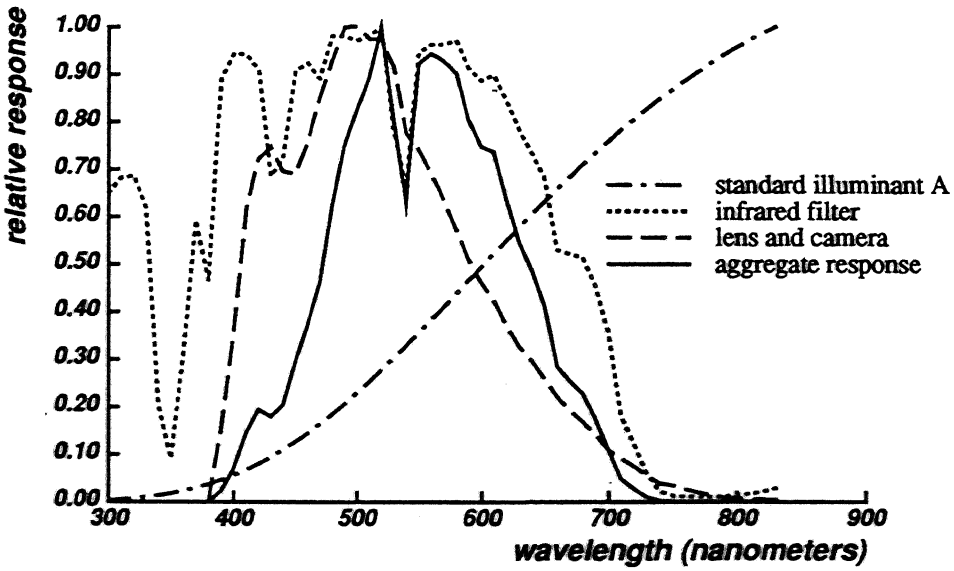

Figure 26: Spectral Curves

We fit P_1 to the experimental data by determining two parameters – the l/d ratio and a scale factor on the four peak magnitudes to account for the scaling effects of the overall light intensity, the lens, the camera, the digitizer, and the FFT. We fit the two parameters using the subroutine "dunlsf" from IMSL, a commercial package of mathematical subroutines in FORTRAN. This subroutine attempts to numerically minimize the sum of squared errors between data and a function by varying the free parameters of the function. From this fit, we determined that $l/d = 0.079$, a physically reasonable value. The resulting fit is shown in Figure 27. We note that P_1 has captured the general downward trend of the data, but has not accounted for all of the variation. This is likely due to a number of effects which we have neglected, such as lens blurring, lens aberrations, and the spatial response of the CCD elements. Also, the two peaks with odd values of n_0 had c_{n_0} close to zero and were very dependent on the value of h, the duty ratio of the grating. Also, as indicated in our experiment with imaging step edges, the camera electronics do not constitute a linear system.

As shown in Figure 27, the data for P_1 extends well beyond the Nyquist frequencies of the

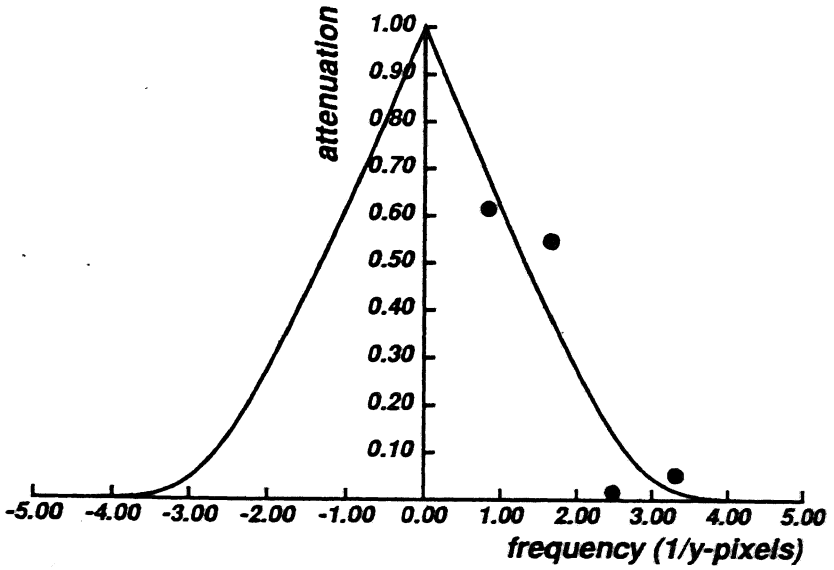

Figure 27: Fitted curve for P_1

CCD, which are 0.29 cycles/y-pixel in the x direction and 0.50 cycles/y-pixel in the y direction. Conventional end-to-end techniques for determining the OTF of digital cameras are Nyquist-limited. Our experiments suggest a new technique for finding OTF's beyond the Nyquist bounds by introducing controlled aliasing.

As our model shows, it is important that the peaks in the Fourier transform be related to their *pre-aliased* frequencies when analyzing the camera's point spread function. It would be a mistake to use the frequencies directly indicated by the Fourier transform, since they have been altered by aliasing. We note that an attempt to fit our P_1 to the aliased data resulted in a squared error of over three times that of the fit for the pre-aliased frequencies and an unreasonable value of l/d.

5.3 Moire Pattern Simulation

We can use our estimates of P_1 and P_2 to model the moire pattern from our experiments. Figure 22 shows our prediction of the moire pattern in the spatial domain. The period and angle of the prediction are about right, as we demonstrated above quantitatively. Figure 24 shows our prediction of the Fourier transform of the moire pattern in Figure 21. As before, we have shown the δ-functions as dots. The peaks in the actual Fourier transform in Figure 23 are spread out due to the finite number of samples in the image.

A more telling visual comparison is to look at the 1-D Fourier transform of a vertical slice through the moire pattern. The dotted curve in Figure 28 was produced by calculating the discrete Fourier transform of each of the columns of the actual moire pattern in Figure 21, then taking magnitudes and averaging. Since each column should differ in phase only, this method allowed us to average random noise effects. The two large spikes represent the obvious moire pattern. Figure 28 also shows our prediction of the same slice. This prediction was made by first calculating the spatial-domain, column profile and then using the same DFT routine that was used on the actual data. We see that the actual data is offset vertically by an almost constant value indicating almost white noise. The predictions on the positions of the peaks is good, as

was demonstrated in the previous section. The amplitude prediction is not as good, indicative of the mediocre fit of P_1 to the amplitude data.

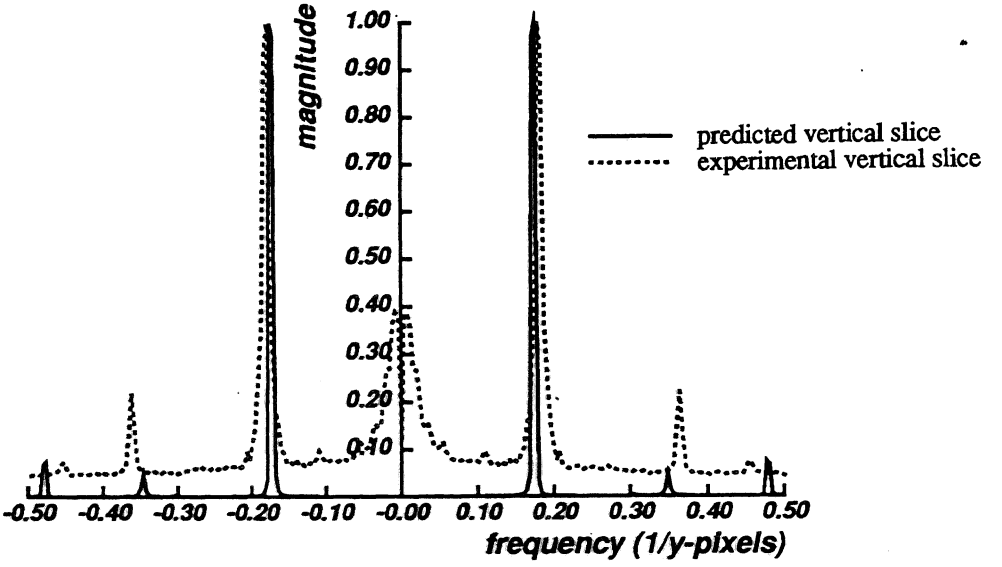

Figure 28: Slices of vertical Fourier transforms

This experiment shows that our sampled-grating, moire pattern model correctly predicts the locations of the frequency peaks. Since the sampling rates of the digitizer $(1/T_{x_2}, 1/T_{y_2})$, were greater than or equal to those of the CCD, no additional aliasing occured in the second sampling stage, and the digitizer sampling rates did not figure explicitly in our predictions. These rates were used implicitly, however, because the final image was sampled at these rates, and we had to account for this in our calculations. Specifically, the distance between adjacent samples along a row in the final image actually represents a distance of $T_{x_2}/T_{x_1} = 0.75$ samples along a row on the CCD. The experiment also shows that our model does a fair job of predicting the amplitudes of the moire pattern. This was especially apparent in the improved fit of P_1 when using the pre-aliased data over using aliased data.

6 Crossed-Gratings Model of Sampled-Grating Moire

We present here a brief experiment to show how an aliased moire pattern can be approximated with crossed gratings. We are prepared to do this at this point because we have determined above the necessary geometric parameters of the actual, aliased moire pattern. Figure 29 shows three superimposed gratings whose periods and angles match those of the CCD camera and grating used in the experiment above. We have made no attempt to impose any particular profile on the three gratings, other than to make the lines thin so they will not run together during reproduction.

According to our analysis in section 4, we can generate a superset of the constituent frequencies of an aliased moire pattern by matching the geometry of the sampling system with crossed gratings. A visual comparison of the crossed gratings in Figure 29 with the aliased moire pattern in Figure 21 shows this to be qualitatively true. The periods and angles of both moire patterns are about equal. In Figure 30 we show the same crossed-gratings model without

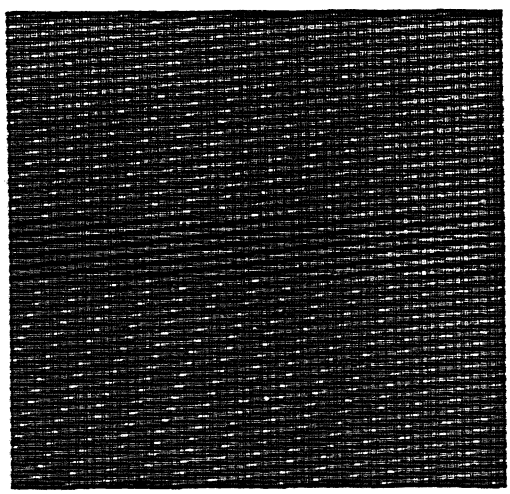

Figure 29: Aliased moire pattern simulated with three crossed gratings

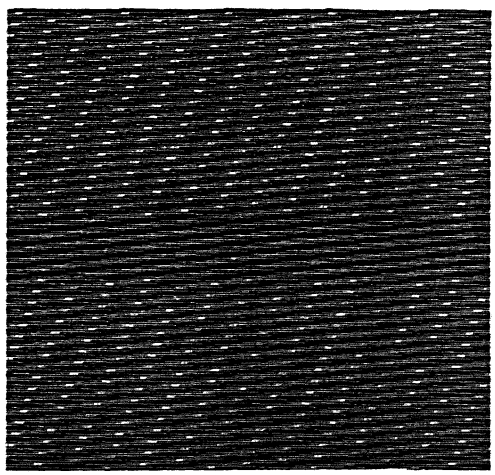

Figure 30: Aliased moire pattern simulated with two crossed gratings

the vertical-line-grating which models the columns of the camera. Essentially the same moire pattern is visible in both. This is to be expected. As we demonstrated in Section 5.1, for our particular set of parameters, the sampling rate in the x direction had virtually no effect on the moire pattern, because the lines of the object grid were almost parallel to the horizontal scanning lines.

7 Conclusion

Past attempts at characterizing sampled-grating moire have used either a crossed-gratings model or a single stage sampling model. We were able to evaluate these models by developing notationally consistent, frequency space models of crossed-grating moire and multiple stage, sampled-grating moire, of which single stage sampling is a special case. In evaluating the crossed-gratings model, we found that if we chose the periods and angles of the crossed gratings to match those of the sampling grid, the resulting crossed-grating moire pattern would contain a superset of the frequencies of the sampled grating. We demonstrated this fact with equations and a simple, qualitative experiment. We also showed that the crossed-gratings model cannot correctly predict the amplitudes of sampled-grating moire.

The single stage, sampled-grating models proposed in the literature are better than the crossed-gratings model for characterizing moire patterns due to aliasing. But we have shown how our model of multiple stage sampling accounts for multiple stages of aliasing, which has a significant impact on both the geometry and brightness of sampled-grating moire patterns. The geometry can become complicated if later sampling stages have lower sampling rates than earlier stages. Thus, in practically applying sampled-grating techniques, it is important to be aware of the sampling

rates of all stages of the imaging system. Otherwise, there could be unanticipated aliasing effects which would likely lead to mistakes in shape measurement. In terms of brightness, we have shown that a single point spread function cannot, in general, characterize a multiple-stage sampling system. We demonstrated with an experiment how our model does a good job of predicting the frequencies present in an actual sampled grating, and a fair job of predicting the amplitudes.

This research demonstrates clearly the justification for using a crossed-gratings model to characterize sampled gratings, but also shows its limitations. We have demonstrated the sorts of errors which can result from a crossed-gratings model or single stage, sampled-grating model, and how these errors can be avoided using our multiple stage, sampled-grating model. The multiple stage sampling model should be used to avoid errors whenever sampling considerations become important in a digital imaging system. A future use of this model might be to increase the sensitivity of moire methods by adjusting the relative sampling rates of the stages of the imaging system.

References

[BK84] Bernard W. Bell and Chris L. Koliopoulos. Moire topography, sampling theory, and charge-coupled devices. *Optics Letters*, 9(5):171–173, May 1984.

[Bry74] Olaf Bryngdahl. Moire: formation and interpretation. *Journal of the Optical Society of America*, 64(10):1287–1294, October 1974.

[CFB85] Maurizio Cetica, Franco Francini, and Duilio Bertani. Moire with one grating and a photodiode array. *Applied Optics*, 24(11):1565–1566, June 1985.

[Gas78] Jack D. Gaskill. *Linear Systems, Fourier Transforms, and Optics*. John Wiley & Sons, 1978.

[Goo68] Joseph W. Goodman. *Introduction to Fourier Optics*. McGraw-Hill, 1968.

[IYS77] Masanori Idesawa, Toyohiko Yatagai, and Takashi Soma. Scanning moire method and automatic measurement of 3-d shapes. *Applied Physics*, 16(8):2152–2162, August 1977.

[MSH88] Yoshihara Morimoto, Yasuyuki Seguchi, and Toshihiko Higashi. Application of moire analysis of strain using fourier transform. *Optical Engineering*, 27(8):650–656, August 1988.

[Pos67] Daniel Post. Sharpening and multiplication of moire fringes. *Experimental Mechanics*, 7(4):154–159, April 1967.

[PYS76] Krzysztof Patorski, Shunsuke Yokozeki, and Tatsuro Suzuki. Moire profile prediction by using fourier series formalism. *Japanese Journal of Applied Physics*, 15(3):443–456, March 1976.

[RK82] Azriel Rosenfeld and Avinash C. Kak. *Digital Picture Processing, Second Edition*. Volume 1, Academic Press, 1982.

[Wil85] David R. Williams. Aliasing in human foveal vision. *Vision Research*, 25(2):195–205, 1985.